

Permeability and elastic properties of rocks from the northern Hikurangi margin: Implications for slow-slip events

Nicola Tisato¹, Carolyn Bland¹, Harm Van Avendonk¹, Nathan Bangs¹, Hector Kevin Garza¹, Omar Alamoudi¹, Kelly Olsen¹, and Andrew Gase¹

¹Affiliation not available

August 22, 2023

Abstract

Fluid flow and pore-pressure cycling are believed to control slow slip events (SSEs), such as those that frequently occur at the northern Hikurangi margin (HM) of New Zealand. To better understand fluid flow in the forearc system, we examined the relationship between elastic properties, compaction, porosity, and permeability of Cretaceous-to-Pliocene sedimentary rocks from the Raukumara peninsula. We found that the permeability of the deep wedge is too low to drain fluids, but fracturing increases permeability by orders of magnitude, making fracturing key for fluid flow. In weeks to months, plastic deformation and clay swelling heal the fractures, restoring the initial permeability. We conclude that overpressures at the northern HM might partly dissipate during SSEs due to enhanced permeability near faults. However, in the weeks to months following an SSE, healing in the prism will lower permeability, forcing pore pressure to rise and a new SSE to occur.

PAPER SUBMITTED TO GEOPHYSICAL RESEARCH LETTERS - AGU

1 **Permeability and elastic properties of rocks from the northern Hikurangi margin:**
2 **Implications for slow-slip events**

3 **Nicola Tisato¹, Carolyn D. Bland^{1*}, Harm Van Avendonk², Nathan Bangs², Hector Garza¹,**
4 **Omar Alamoudi¹, Kelly Olsen^{2†}, Andrew Gase^{2‡}**

5 ¹ Department of Earth and Planetary Sciences, Jackson School of Geosciences, The University of
6 Texas at Austin, Austin, TX, U.S.

7 ² Institute for Geophysics, Jackson School of Geosciences, The University of Texas at Austin,
8 Austin, TX, U.S.

9 * Now at: Pariveda Solutions, Dallas, TX, U.S.

10 † Now at: Descartes Labs, 1607 Paseo de Peralta, Suite B, Sante Fe, NM, U.S.

11 ‡ Now at: Geology Department, Western Washington University, Bellingham, WA, U.S.

12
13 Corresponding author: Nicola Tisato (nicola.tisato@jsg.utexas.edu)

14 **Key Points:**

- 15 • Elastic properties, plastic deformation, and permeability of northern Hikurangi margin
16 rocks
- 17 • Permeability-porosity relationship in accretionary prisms
- 18 • Clay swelling and plastic deformation controls permeability healing, providing a
19 mechanism justifying slow-slip event cyclicality
20

21 **Abstract**

22 Fluid flow and pore-pressure cycling are believed to control slow slip events (SSEs), such
23 as those that frequently occur at the northern Hikurangi margin (HM) of New Zealand. To better
24 understand fluid flow in the forearc system, we examined the relationship between elastic
25 properties, compaction, porosity, and permeability of Cretaceous-to-Pliocene sedimentary rocks
26 from the Raukumara peninsula. We found that the permeability of the deep wedge is too low to
27 drain fluids, but fracturing increases permeability by orders of magnitude, making fracturing key
28 for fluid flow. In weeks to months, plastic deformation and clay swelling heal the fractures,
29 restoring the initial permeability. We conclude that overpressures at the northern HM might partly
30 dissipate during SSEs due to enhanced permeability near faults. However, in the weeks to months
31 following an SSE, healing in the prism will lower permeability, forcing pore pressure to rise and
32 a new SSE to occur.

33

34 **Plain Language Summary**

35 Earth's crust is composed of many tectonic plates fitting together like jigsaw puzzle pieces.
36 Tectonic plates subduct in the mantle along active converging margins, where the forces driving
37 such a convergence can trigger large earthquakes. However, these subduction zones often deform
38 without producing earthquakes, but through slow-slip. The Hikurangi Margin (HM) of New
39 Zealand is a well-studied subduction zone, producing both earthquakes and slow-slip events. The
40 northern HM exhibits more frequent and shallower slow-slip events than the southern margin.
41 Understanding what controls such differences can help improve the general understanding of
42 subduction zone fault mechanics and earthquakes. One of the hypotheses is that the differences
43 between the deformation of the northern and southern HM are controlled by the pore pressure at
44 depth. We tested the elastic and fluid-transport properties of four samples from the northern HM
45 and found that the overriding plate, if not fractured, would be impermeable to fluids. We also
46 tested a fractured sample and observed efficient healing that resets the initial permeability. We
47 conclude that fracturing the overriding plate is fundamental to draining the fluids carried at depth
48 by the subducting plate, and slow-slip events may create new pathways for fluids to escape to the
49 seafloor.

50

51 **1 Introduction**

52 At the shallow (<15 km depth) portion of the plate interface of subduction zones, scientists
53 have found that convergence between the tectonic plates is often accommodated by modes of slip
54 in between fast earthquakes and aseismic creep (Saffer & Wallace, 2015). Slow-slip events (SSEs)
55 represent one class of such transient phenomena, which can lead to several centimeters of slip over
56 several days to months (Schwartz & Rokosky, 2007). The relatively large seismic moment released
57 by shallow SSEs, comparable to that of earthquakes (Passarelli et al., 2021), proves the importance
58 to understand SSEs and how they influence the seismogenic character of a convergent margin.
59 Frictional properties and stress heterogeneities along the plate interface might favor SSEs (Barnes
60 et al., 2020; Bell et al., 2010; Im et al., 2020; Rabinowitz et al., 2018). Subducting oceanic crust
61 and sediments release large volumes of fluids (i.e., seawater and CO₂) whose pressure can exceed
62 hydrostatic conditions when confined within low permeability rocks, lowering the effective stress

63 on the shallow megathrust or splay faults and creating conditions conducive to SSEs (Kitajima &
64 Saffer, 2012; Tsuji et al., 2008; Warren-Smith et al., 2019).

65 The northern Hikurangi margin (HM) of North Island, New Zealand, is a subduction zone
66 with a shallow forearc and plate interface, where sediment accretion, compaction, and deformation
67 have been modulated for millions of years by underthrusting seamounts (Gase et al., 2021; Sun et
68 al., 2020). Subducting topography (e.g., seamounts) may cause stress heterogeneities (Bangs et al.,
69 2023; Leah et al., 2022; Sun et al., 2020) and fluid pressure transients (Shaddox & Schwartz, 2019)
70 that can lead to SSEs, several of which have been characterized in great detail by onshore geodetic
71 and offshore absolute pressure gauge (APG) data (Yohler et al., 2019). Offshore Gisborne SSEs
72 occur every 1-2 years and can last several weeks, during which 5 to 30 cm of slip may be
73 accommodated (Wallace, 2020). Temporal variations in the character of earthquake focal
74 mechanisms within the subducting oceanic crust provide compelling evidence for low effective
75 stress before an SSE (Warren-Smith et al., 2019). This observation suggests that increases in fluid
76 pressure enable SSEs and that the slip itself is accompanied by fluid release. Nevertheless, fluid
77 transport through the accretionary wedge in this deformation cycle is not yet well understood
78 (Antriasian et al., 2018).

79 The physical properties of accreted sediments of the northern HM and their relationship to
80 slip phenomena have been studied recently with the use of cores and data from IODP expeditions
81 (e.g., Wallace et al., 2019). The resulting studies have shed new light on the frictional properties,
82 shallow dewatering, and faulting near the seafloor (Aretusini et al., 2021; Boulton et al., 2019,
83 2022; Dutilleul et al., 2021; Fagereng et al., 2019; French & Morgan, 2020; Shreedharan et al.,
84 2022). However, to understand how fluid flow and deformation interplay in the deeper prism, we
85 also must consider the physical properties of older, compacted, and diagenetically mature strata
86 (Bland et al., 2015, Bassett et al., 2022). Here we present and discuss laboratory testing performed
87 on rock samples from the subaerial northern HM as proxies of deep rocks in the prism to better
88 understand fluid transport within the subduction zone.

89 **2 Materials and Method**

90 To test the compaction, elastic, and transport properties of rocks from the northern HM,
91 we collected and performed experiments on outcrop samples from the Raukumara peninsula (Figs
92 1, S1) presenting different ages and degrees of diagenesis. In the central part of the peninsula, we
93 collected a fine-grained sandstone from the Jurassic-to-Early Cretaceous Torlesse Supergroup
94 forming the backstop for the accretionary wedge (sample MO02) (Adams & Graham, 1996;
95 Mortimer et al., 2014). Just east of sample MO02 location, we sampled a calcareous fine-grained
96 sandstone with a silty matrix from the Late Cretaceous-to-Paleocene Tinui Group (sample MT07)
97 that likely represents an early passive margin deposit, now deeply buried in the accretionary wedge
98 (Mortimer et al., 2014). Closer to the East coast, we collected a siltstone (sample GB13) from the
99 middle Miocene Tolaga Group, which was deposited in slope basins after subduction initiated
100 along the HM (van de Lagemaat et al., 2022), and a glauconitic fine-grained sandstone (sample
101 FB12) from the Pliocene Mangaheia Group.

102 We determined mineral abundances and assemblages of each sample through X-ray
103 diffraction (XRD) analyses and transmitted light microscopy by preparing 30 μm in thickness thin-
104 sections. To estimate density, porosity, compressional and shear ultrasonic wave velocities (i.e.,
105 V_p and V_s), and helium gas permeability, we prepared cylindrical core plugs with parallel end
106 faces for each sample. Samples were tested at the UT Austin Rock-Deformation-Laboratory for
107 confining pressures (P_c) up to 200 MPa (~ 12.5 km depth for hydrostatic pore pressure and

108 overburden density of 2.6 g/cm³) and deviatoric vertical force (F_v) ~2.6 kN. Each core plug was
 109 mounted inside a PVC jacket and between two core holders equipped with ultrasonic transducers
 110 and fluid ports, which are used to saturate and measure the core permeability. This sample
 111 assembly is mounted inside the triaxial cell (NER Autolab 1500) between the load cell and the
 112 vertical force piston. We define the mean stress as $\sigma_M = \frac{\sigma_1 + \sigma_2 + \sigma_3}{3}$, where $\sigma_2 = \sigma_3 = P_c$ and σ_1 is
 113 the maximum vertical stress: $\sigma_1 = \sigma_d + P_c$, where $\sigma_d = \frac{F_v}{A}$ is the deviatoric stress, and A is the
 114 sectional area of the core plug. We also define effective stress (σ') as the difference between the
 115 mean stress and the pore pressure: $\sigma' = \sigma_M - P_p$.

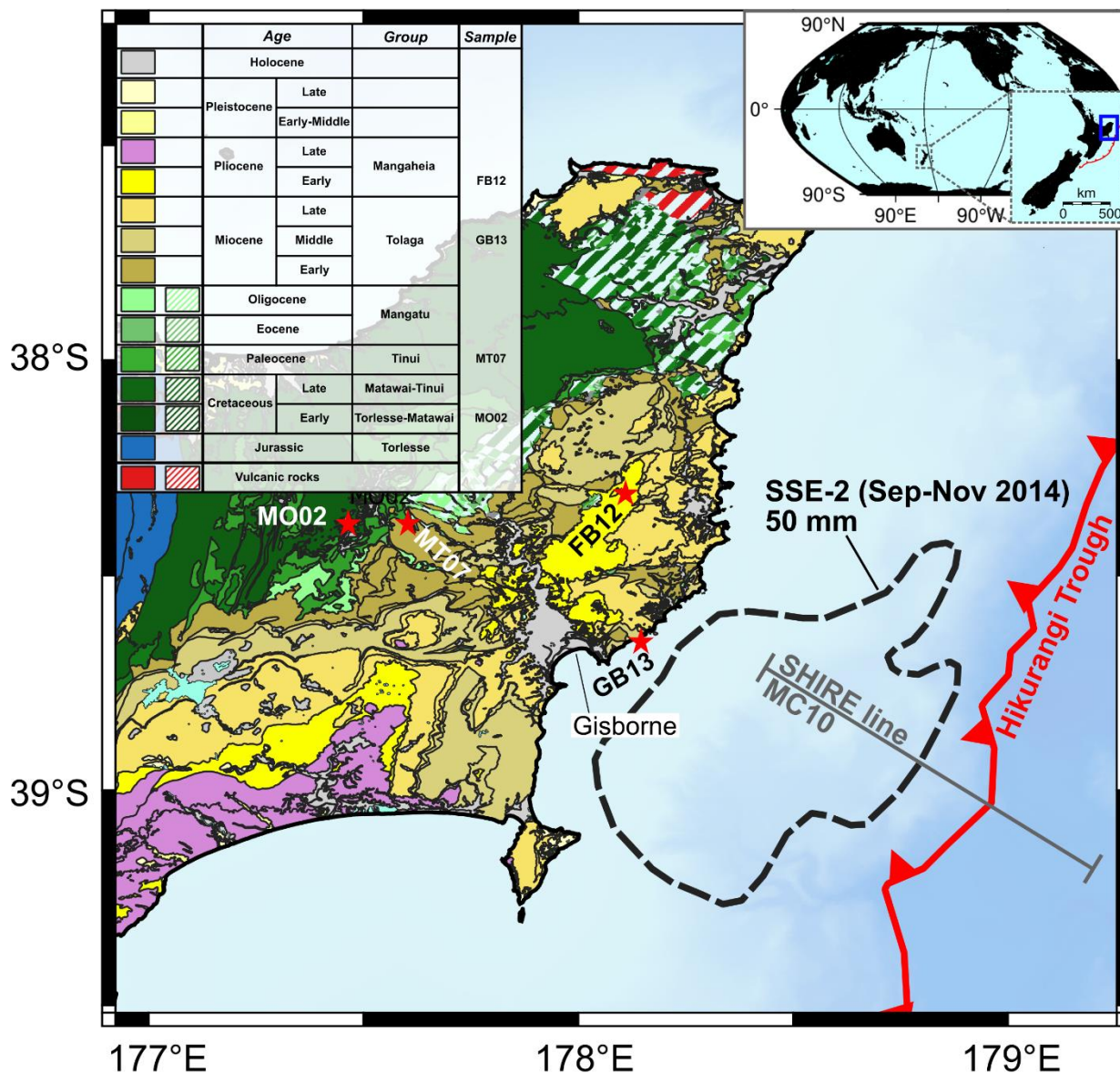
116 We measured ultrasonic velocities using the transmission method at room temperature and
 117 a frequency of ~800 kHz (Birch, 1960). To understand the effect of saturation on V_p and V_s , we
 118 measured the ultrasonic velocities of sample GB13 saturated with water previously chemically
 119 equilibrated with the sample. During 30 hours, we recorded the injection of 4.7 ml of this fluid,
 120 equivalent to 136% of GB13 pore-space volume.

121 Sample permeabilities were calculated through the transient method measuring the pressure
 122 equilibration of the helium gas contained in two volumes connected to the sample end-faces and
 123 flowing through the sample (Sutherland & Cave, 1980). To understand the effect of porosity
 124 reduction on the permeability of young, loosely consolidated rocks, we measured FB12
 125 permeability before and after mechanical compaction, which was assumed to be isotropic. First,
 126 we measured ultrasonic velocities and permeabilities at P_c up to 70 MPa and $\sigma_d = 5$ MPa, then,
 127 we increased P_c stepwise to 100, 150 and 200 MPa and waited for 19, 24 and 5 hours to measure
 128 creep until the observed shortening rate was less than 1 $\mu\text{m}/\text{hour}$. Finally, we measured the sample
 129 permeability for varying P_c up to 200 MPa.

130 To study how fractures influence the permeability of HM rocks, we split sample MT07
 131 through a Brazilian test producing a sub-vertical fracture connecting the opposite end-faces of the
 132 core plug. Then, to study the effect of stress on permeability healing, we kept the sample dry and
 133 measured permeability as a function of σ' and we collected three micro-computed tomographies
 134 (μCT) to seek evidence of variations in fracture aperture. A detailed chronology of the operations
 135 follows: On day 1, after the Brazilian test, we collected μCT dataset S1. Between day 2 and 9 we
 136 performed the first permeability test (kT1) for σ' between 24 and 65 MPa. During kT1 (days 3 to
 137 5) we promoted healing by keeping σ' to 65 MPa. After kT1 and for the next 39 days, the sample
 138 remained inside the pressure vessel at $\sigma' \sim 0$ MPa. Between day 48 and day 77, we performed the
 139 second permeability test (kT2) at σ' ranging 5.6 to 64 MPa. At the end of kT2 we removed the
 140 sample from the pressure vessel and acquired μCT dataset S2. Then, the jacketed sample was
 141 placed inside a humidity-controlled chamber equipped with a water container and a thermo-
 142 hygrometer. For 72 hours, a medium to low vacuum (<0.5 bar) was maintained to promote water
 143 evaporation, causing the chamber relative humidity to remain above 97% and activating clays such
 144 as smectites with pronounced swelling properties (Villar et al., 2005). Finally, we acquired μCT
 145 dataset S3, and produced a thin section perpendicular to the sample axis. On the thin section, we
 146 examined the morphology of the fracture for evidence of clay infilling, possibly caused by plastic
 147 deformation and triggered by clay swelling.

148 Each μCT dataset comprises 1600, 33.3 μm resolution, 16-bits TIFF images perpendicular
 149 to the sample axis, recording the entire sample except 4.37 mm at the top and bottom. After
 150 normalization and segmentation, we calculated fracture apertures (B) for each CT dataset by
 151 producing fracture aperture distribution projections (FADP) whose mean and standard deviation

152 provided average apertures (B_m) and associated uncertainties. We report more details on the
 153 methods in the supporting information.



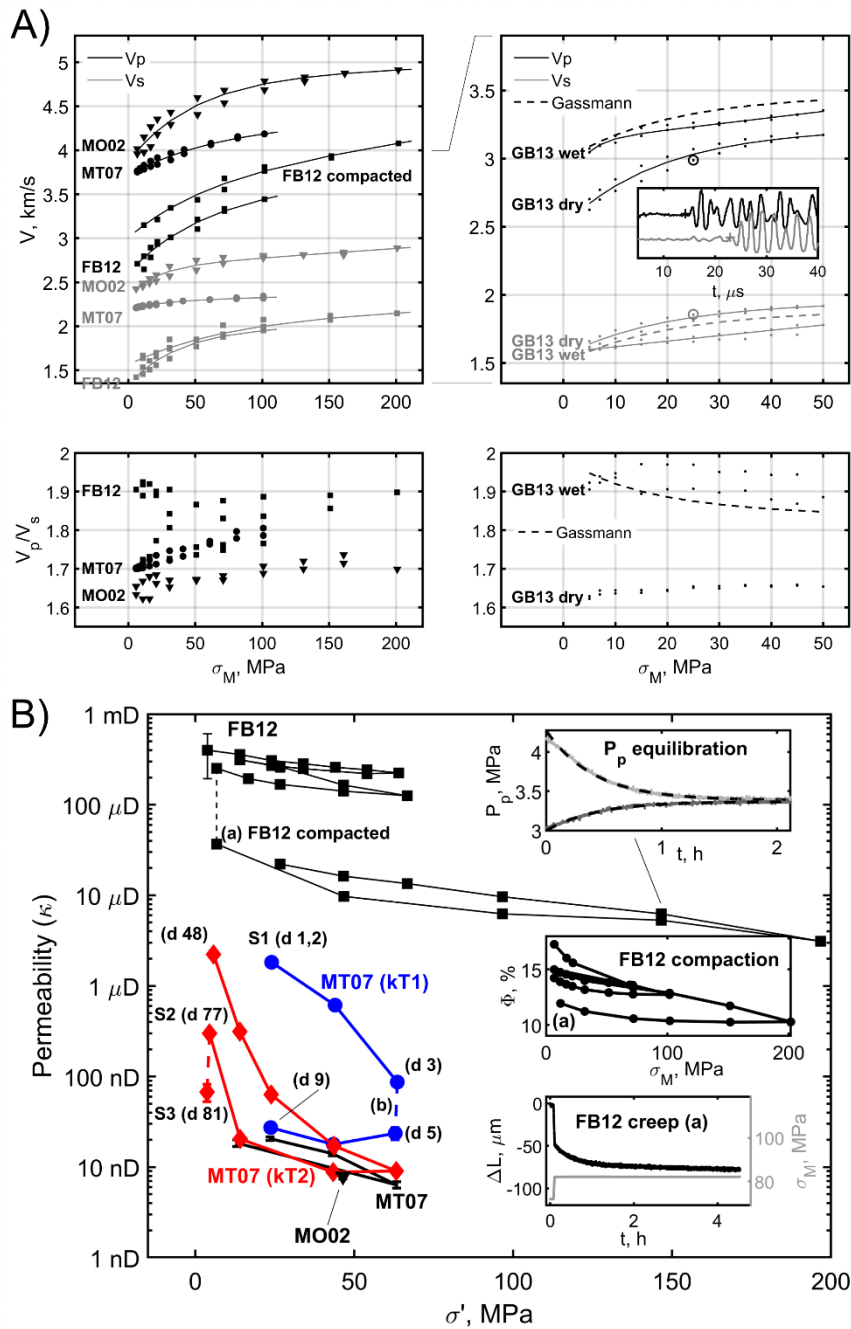
154 177°E 178°E 179°E
 155 **Figure 1. Geologic map of the Raukumara peninsula with the position of the rock samples**
 156 **used in this study (Mazengarb & Speden, 2000). The offshore dashed line contour marks the**
 157 **50 mm geodetic slip model for the September-November 2014 SSE (Warren-Smith et al.,**
 158 **2019). The offshore line indicates the seismic line MC10 from the SHIRE project (Gase et**
 159 **al., 2021).**

160 **3 Results**

161 The four samples (Fig S1) contain more than 35 wt% quartz and feldspars. The remaining
 162 minerals are calcite, and clays: chlorite, kaolinite, micas, illite, and smectite group minerals (Fig
 163 S2). Clays and swelling clays (i.e., illites and smectites) represent at least 24 wt% and 13 wt%,

164 respectively (Fig S3). Porosities vary between 7 and 18%, where the tighter samples (MT07 and
165 MO02) have a longer diagenetic or metamorphic history. Microphotography reveals that the grain
166 size varies significantly among the four samples: Sample GB13 has the smallest grain size (<20
167 μm).

168 Ultrasonic velocity measurements (Fig 2A) show that V_p and V_s increase with σ_m , and the
169 younger samples (FB12 and GB13) generally have lower wave speeds. V_p to V_s ratios vary
170 between 1.6 and 1.95, with the least consolidated and youngest sample (FB12) exhibiting the
171 highest values. After saturation, sample GB13 V_p increased by ~ 250 m/s on average while V_s
172 decreased by ~ 100 m/s on average, increasing the V_p to V_s ratio from ~ 1.65 to ~ 1.95 .



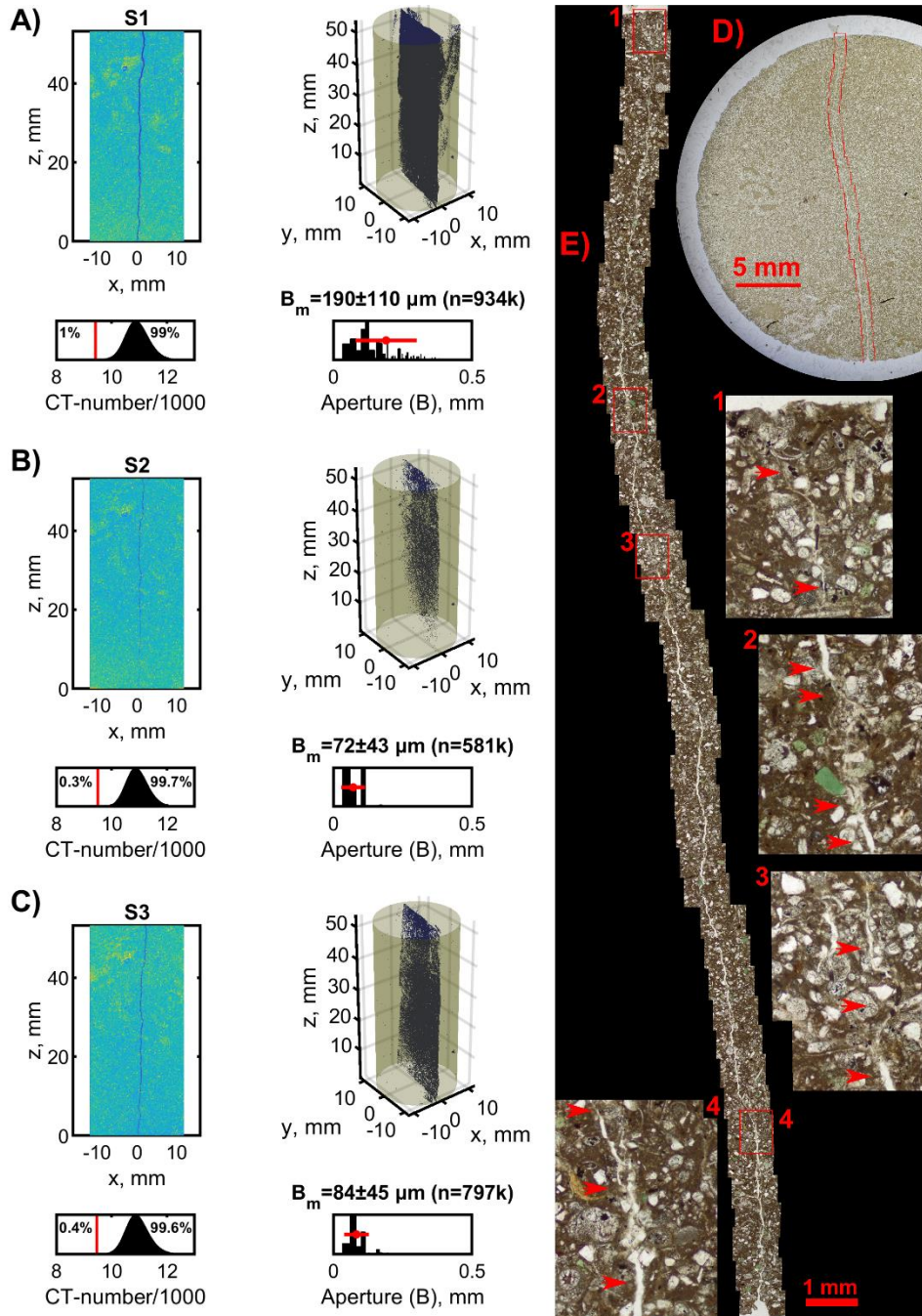
173 **Figure 2. A) Left-top panel: ultrasonic velocities measured on the samples MO02, MT07 and**
 174 **FB12 as a function of σ_M . Right-top panel: ultrasonic V_p and V_s for sample GB13 when dry**
 175 **and saturated with water. Dashed lines indicate the theoretical saturated velocities from**
 176 **Gassmann fluid substitution (Gassmann, 1951). The inset shows examples of P and S**
 177 **waveforms recorded for the dry sample at the conditions indicated by the circled dots.**
 178 **Bottom panels: V_p to V_s ratios for the laboratory data and the fitting curves reported in the**
 179 **panels above. B) Permeabilities for samples FB12, MT07, and MO02 as a function of σ' . (a)**
 180 **“FB12 compaction” reports the loss of permeability due to the step-by-step increase of σ' ;**
 181 **partial compaction and loss of porosity in sample FB12 are shown in “FB12 creep” and**

182 **“FB12 compaction” insets, respectively. "Pp equilibration" inset: example of pore pressure**
183 **(Pp) equilibration and fitting curves (dashed lines). The blue and red curves show the**
184 **permeability of the fractured sample MT07 during the two permeability cycles (kT1 and kT2).**
185 **(d X) near data points indicates X days since stage S1 (Fig 3A). Day 77 was the end of kT2**
186 **and stage S2 (Fig 3B): the sample was CT-scanned and exposed to a humid atmosphere for**
187 **72 hours. Day 81 was stage S3: we CT-scanned and remeasured the sample permeability (Fig**
188 **3C,D,E).**

189 Before compaction, sample FB12 permeability ranged between 200 and 400 μD . Then, we
190 raised P_c twice to 70 MPa, causing the permeability to decrease by a factor of two and porosity by
191 3% (i.e., at $\sigma_m \sim 7$ MPa, porosity varied from 17.3 to 14.2%). In the following two cycles, where P_c
192 reached 200 MPa, porosity decreased to 13.9%, and the permeability declined by almost an order
193 of magnitude. Concurrently, the ultrasonic V_p increased from 2.6 km/s to 4 km/s.

194 Samples MO02 and MT07, when intact, have permeabilities below 100 nD, regardless of
195 σ' . The permeability of the fractured MT07 evolved between stages S1, S2, and S3. After S1 and
196 during the permeability cycle kT1, the permeability dropped from 2 μD to 87 nD. After exposing
197 the sample to $\sigma' \sim 65$ MPa for more than 48 hours (Fig 4B b), we continued kT1 and found that the
198 permeability further decreased to 24 nD. The permeability remained ~ 2 orders of magnitude lower
199 than the initial permeability, i.e., around 30 nD, when σ' was reduced. After 39 days, the new
200 increase of σ' during the second permeability cycle kT2, caused the permeability to drop to 9 nD.
201 During the following decrease of σ' , the permeability resembled pre-fracturing values. The last
202 measurement of kT2 was performed at $\sigma' = 4.5$ MPa and permeability was 300 nD, seven times
203 lower than the initial value measured at $\sigma' = 5.6$ MPa. After exposing the sample to humidity for 72
204 hours, the permeability, measured at $\sigma' = 3.7$ MPa, decreased to 67 nD.

205 CT-scans visual inspection and analyses reveal the variation of B_m that varied from 190 \pm
206 110, to 72 \pm 43 and 84 \pm 45 μm during the stages S1, S2, and S3, respectively (Fig 3A,B,C).
207 During the same stages, the number of voxels counted within the fracture varied respectively from
208 $\sim 934,000$ to $\sim 581,000$ and $\sim 797,000$. Microphotography of sample MT07 at stage S3, shows that
209 in several loci, the fracture collapsed, and a fine-grained amorphous mass infilled the fracture (Fig
210 3D,E). These observations suggest that varying confining pressure and humidification caused clay
211 minerals plastic deformation and swelling, partially closing the fracture and reducing the
212 permeability.



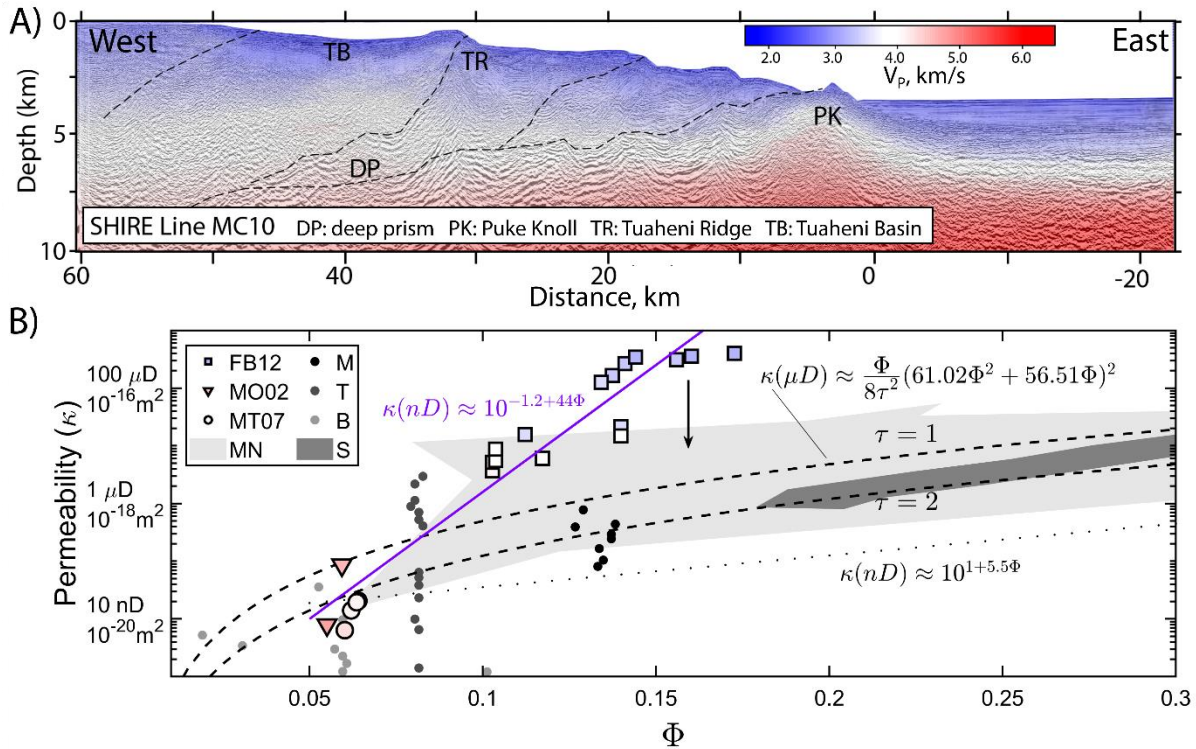
213 **Figure 3.** CT-scan and transmitted light microphotography of sample MT07 after
 214 fracturing. A, B, and C are CT-scans at stages S1, S2, and S3, respectively. Each top-left inset
 215 in these panels reports a section of the CT-scan model after normalization. CT-number
 216 distribution is shown in the bottom-left inset. The red vertical line indicates t_x (eq. S5). The
 217 percentages on the left and right of the red line indicate the relative quantity of voxels
 218 representing air and solid rock, respectively. The right top inset in each panel shows the
 219 binarized 3D model, where voxels collected within the fracture are blue. The bottom right
 220 inset show the aperture distribution (B), the calculated average and standard deviation (B_m
 221 and horizontal red bar), and the total count of voxel within the fracture (n). Panel D is a

222 **microphotography of the thin section at stage S3. Panel E reports zooms from panel D. Insets**
223 **1 to 4 show fracture infill, which are highlighted by red arrows along with open fractures.**

224 **4 Discussion**

225 We provide porosity-permeability relationships for rock samples from the subaerial
226 northern HM under a range of confining pressures. Ultrasonic velocities of dry samples are similar
227 to the seismic velocities estimated offshore New Zealand by the SHIRE project (Gase et al., 2021).
228 The seismic reflectivity imaged along the transect MC10 shows the decollement along the prism
229 base and several splay faults that may partly accommodate the convergence (Fig 4A). Inside the
230 prism, V_p increases gradually from 2.0 km/s near the surface to 4.5 km/s at the prism base ~7 km
231 below sea level. In Fig 4B, the comparison between the seismic and ultrasonic velocities suggests
232 that sample FB12, and possibly also sample GB13, represent the modern slope basins on the outer
233 prism, which is consistent with their depositional environment. The ultrasonic velocities of sample
234 MT07 of the Tinui Group correspond well to the velocities of the deep part of the prism, where
235 V_p reaches 4.5 km/s. Compaction and diagenesis must contribute to the increase of V_p with depth
236 (Dvorkin & Nur, 1996; Saxena & Mavko, 2014). We measured an ultrasonic V_p of 4.8 km/s at
237 150 MPa in the Torlesse basement sample MO02, which is higher than what we imaged in the
238 deep prism on Line MC10 (Fig 4), suggesting that there may not be a deep offshore portion of the
239 Torlesse basement offshore northern HM (Bassett et al., 2022; Gase et al., 2021).

240 Our comparison between seismic and ultrasonic velocities in Figure 4 is semi-quantitative
241 as uncertainty is introduced by microcracks produced during sample preparation – see SI for details
242 (Eberhart-Phillips et al., 1989; Tsuji & Iturrino, 2008), and by frequency differences. Velocities in
243 section MC10 and on our samples have been measured at frequencies around 20 Hz and 800 kHz,
244 respectively. Considering the frequency range, a typical P-wave quality factor ranging from 30 to
245 150, and a nearly-constant Q model (Liu et al., 1976; Tisato et al., 2021), we should expect a
246 velocity dispersion between 2.3 and 12%. Conversely, SHIRE and laboratory data were collected
247 on saturated and dry samples, respectively. Saturation increases P-wave velocities of sample GB13
248 by 5 to 15%, suggesting that the effects of fluid saturation and anelasticity on velocities should
249 counteract each other. Given the similarity in P-wave velocities and depositional environment, we
250 suggest that the Tinui and Tolaga group rocks (samples MT07 and GB13) are good lithological
251 proxies for the deep and shallow offshore Hikurangi prism, respectively.



252 **Figure 4. A) Velocity model along the SHIRE Line MC10 (Gase et al., 2021). B) Summary of**
 253 **laboratory result: permeabilities vs porosity and color-coded markers (colorbar in panel A)**
 254 **as a function of ultrasonic V_p for samples FB12, MO02, and MT07 (Tables S1 and S2). The**
 255 **arrow indicates in which direction the permeabilities vary when tests are performed using**
 256 **water rather than helium gas. Dashed lines indicate empirical permeability vs porosity**
 257 **according to eq. 3. The dotted line represents an average permeability for unconsolidated**
 258 **clays and possibly a lower bound for the permeability of HM sediments (Neuzil, 1994). S data**
 259 **(dark-gray area) are for siltstones (Reece et al., 2012). The continuous line fits our data and**
 260 **agrees with measured mudstone permeabilities indicated by the MN gray-shaded area**
 261 **(Magara, 1978; Neglia, 1979). Such a line also represents an upper bound for the**
 262 **permeability of HM rocks. M, T, and B data are permeabilities measured in boreholes: M**
 263 **by Reisdorf et al. (2016), Yu et al. (2017); T by Boisson et al. (2001); B by Intera Eng. Ltd.**
 264 **(2011), Roberts et al. (2011), Walsh (2011).**

265 The permeability of our samples ranges from 1 nD to 1 mD, with the samples representing
 266 the deep part of the prism being the tightest. Neuzil (1994, 2019) compiled data from several
 267 studies on unconsolidated clays with a maximum porosity of 80%, and a few consolidated
 268 mudstone-siltstones with porosities (Φ) <35%. Saffer & Bekins (1998) followed Neuzil's work
 269 and described the permeability (κ) of the Nankai accretionary complex as:

270
$$\kappa(nD) \approx 10^{1+5.5\phi} \quad \text{eq. 1}$$

271 Equation 1 fits the porosity-permeability relationship of unconsolidated sediments and is a lower
 272 bound for the permeability of mudstones that are similar to our samples (Magara, 1978; Neglia,
 273 1979; Reece et al., 2012). On the other hand, we found that:

274 $\kappa(nD) \approx 10^{-1.2+44\phi}$ eq. 2

275 fits our results and is an upper bound for the permeability of mudstones. We suggest that the
 276 permeabilities calculated from equations 1 and 2 (Fig 4B) overestimate permeabilities in the
 277 Northern Hikurangi accretionary prism at depths >1 km because helium gas is not as efficient as
 278 seawater in activating swelling clays whose expansion lowers the effective permeabilities (Villar
 279 et al., 2005); At burial depths >1-2 km, the porosity of clay-bearing sediments, mudstones,
 280 siltstone, and shales drops below 35% (Griffiths & Joshi, 1989; Magara, 1978; Skempton, 1969);
 281 Permeabilities measured in boreholes are typically orders of magnitude higher than those measured
 282 in the laboratory due to the presence of fractures (Fig 4B lines M,T,B) (Neuzil, 2019), and
 283 numerical models of permeability in microfractured claystones agree with the mudstone porosity-
 284 permeability in Fig 4B (Vora & Dugan, 2019). We also propose that the permeability of rocks in
 285 the Northern Hikurangi accretionary prism can be described by a Kozeny-Carman relation (dashed
 286 lines in Fig 4B):

287 $\kappa = \frac{\phi}{8\tau^2} R^2$ eq. 3

288 Where τ is tortuosity, and R is the median pore diameter (Carman, 1997). We obtained $R(nm) =$
 289 $61.02\phi^2 + 56.51\phi$ from data reported by Hunt (1996) for similar lithologies.

290 Every 1-2 years, the northern HM experiences an SSE that lasts several weeks (Wallace,
 291 2020). Recent analyses of the APG data offshore Gisborne have shown that the 2014 SSE may
 292 have experienced up to 30 cm of slip in the center of a ~100 km wide patch, though less
 293 displacement is expected along the edges (Yohler et al., 2019). Some authors have suggested that
 294 SSEs that originate along the decollement at the base of the wedge are accompanied by slip
 295 diverted to thrust faults in the Hikurangi accretionary wedge (Shaddox & Schwartz, 2019). We
 296 expect SSEs to deform and fracture the rocks along these thrust faults (Morgan et al., 2022). Our
 297 laboratory measurements before and after rock failure for sample MT07 show that the deeper
 298 prism, where Tinui Group equivalent rocks may be present, may experience large increases in
 299 permeability during an SSE.

300 In a few weeks, the fractured sample MT07 regained its pre-fracturing permeability.
 301 Between stages S1 and S2, the permeability recovery was achieved in dry conditions. Although
 302 sample MT07 and sample FB12 have different compaction levels and grain sizes, they share
 303 similar mineralogy. Thus, although limited, we expect plastic deformation also in sample MT07,
 304 likely concentrated near clays (Mondol et al., 2008). Between stages S2 and S3, the permeability
 305 decreased by a factor of 5 while B_m increased, suggesting clay expansion. Once confined, we
 306 expect that the hydrated clays would deform plastically, clogging the fracture more efficiently than
 307 dry clays and justifying the permeability loss. We propose that permeability healing is also present
 308 along HM faults, given the presence of clays at depth, especially above the 5-7 km deep
 309 temperature-controlled smectite-illite transition (Antriasian et al., 2018; Freed & Peacor, 1989;
 310 Pecher et al., 2017; Tisato & Marelli, 2013).

311 In the Hikurangi subduction zone, fluids expelled from pore space and fluids released by
 312 dehydration reactions travel along the plate interface or through the accretionary wedge (Ellis et
 313 al., 2015). As the fluid pressure increases near the decollement and inside the accretionary wedge,
 314 conditions may become favorable for an SSE (Burgreen-Chan et al., 2016; Kobayashi & Sato,

315 2021). Though this mechanism has been proposed for several subduction zones where SSE occur
316 at larger depths (Audet et al., 2009; Kodaira et al., 2004), the analysis of Warren-Smith et al.
317 (2019) on the northern HM, is also compatible with the sealing of fluid pathways after an SSE.
318 The expansion and plastic deformation of clays may provide an efficient mechanism to reduce
319 permeability over weeks or months after an SSE.

320 Permeability healing, favoring the development of overpressures, reconciles with the poor
321 mechanical healing shown by Shreedharan et al. (2023),_hindering elastic energy accumulation,
322 because both set conditions conducive to SSEs.

323 **5 Conclusions**

324 We provided relationships between porosity, permeability, and confining pressure for
325 rocks that make up the accretionary prism of the northern HM. We suggest an empirical porosity-
326 permeability relationship to model fluid transport and estimate effective stress in shallow
327 subduction zones. Mechanical failure of these rocks enhances permeability, but over the course of
328 several weeks, healing reduces the permeability again, suggesting that after an SSE, sediments
329 deep in the northern HM accretionary prism can recover permeability efficiently within the time
330 frame of an SSE as a mechanism explaining the regular recurrence of these events.

331 **Acknowledgments**

332 We thank Lucy Flesh, Carolyn Boulton, and one anonymous reviewer for the insightful reviews,
333 Luc Lavier and Dominic Strogon for the valuable discussions. NSF supported this research (grant
334 OCE-1949171).

335 **Open Research**

336 Data are publicly available upon publication at <https://doi.org/10.18738/T8/RMXMIQ> or can be
337 requested to the corresponding author.

338 **References**

- 339 Adams, C. J., & Graham, I. J. (1996). Metamorphic and tectonic geochronology of the Torlesse
340 Terrane, Wellington, New Zealand. *New Zealand Journal of Geology and Geophysics*,
341 *39*(2), 157–180. <https://doi.org/10.1080/00288306.1996.9514703>
- 342 Antriasian, A., Harris, R. N., Tréhu, A. M., Henrys, S. A., Phrampus, B. J., Lauer, R., et al.
343 (2018). Thermal Regime of the Northern Hikurangi Margin, New Zealand. *Geophysical*
344 *Journal International*. <https://doi.org/10.1093/gji/ggy450>

- 345 Aretusini, S., Meneghini, F., Spagnuolo, E., Harbord, C. W., & Di Toro, G. (2021). Fluid
346 pressurisation and earthquake propagation in the Hikurangi subduction zone. *Nature*
347 *Communications*, 12(1), 2481. <https://doi.org/10.1038/s41467-021-22805-w>
- 348 Audet, P., Bostock, M. G., Christensen, N. I., & Peacock, S. M. (2009). Seismic evidence for
349 overpressured subducted oceanic crust and megathrust fault sealing. *Nature*, 457, 76–78.
350 <https://doi.org/10.1038/nature07650>
- 351 Bangs, N. L., Morgan, J. K., Bell, R. E., Han, S., Arai, R., Gase, A. C., et al. (2023). Slow slip
352 along the Hikurangi margin linked to fluid-rich sediments trailing subducting seamounts.
353 *Nature Geoscience*, IN PRESS.
- 354 Barnes, P. M., Wallace, L. M., Saffer, D. M., Bell, R. E., Underwood, M. B., Fagereng, A., et al.
355 (2020). Slow slip source characterized by lithological and geometric heterogeneity.
356 *Science Advances*, 6(13). <https://doi.org/10.1126/sciadv.aay3314>
- 357 Bassett, D., Arnulf, A., Henrys, S., Barker, D., Avendonk, H., Bangs, N., et al. (2022). Crustal
358 Structure of the Hikurangi Margin From SHIRE Seismic Data and the Relationship
359 Between Forearc Structure and Shallow Megathrust Slip Behavior. *Geophysical Research*
360 *Letters*, 49(2). <https://doi.org/10.1029/2021GL096960>
- 361 Bell, R., Sutherland, R., Barker, D. H. N., Henrys, S., Bannister, S., Wallace, L., & Beavan, J.
362 (2010). Seismic reflection character of the Hikurangi subduction interface, New Zealand,
363 in the region of repeated Gisborne slow slip events. *GJI*, 180, 34–48.
364 <https://doi.org/10.1111/j.1365-246X.2009.04401.x>
- 365 Birch, F. (1960). The velocity of compressional waves in rocks to 10 kilobars: 1. *Journal of*
366 *Geophysical Research*, 65(4), 1083–1102. <https://doi.org/10.1029/JZ065i004p01083>

- 367 Bland, K. J., Uruski, C. I., & Isaac, M. J. (2015). Pegasus Basin, eastern New Zealand: A
368 stratigraphic record of subsidence and subduction, ancient and modern. *NZJGG*, 58, 319–
369 343. <https://doi.org/10.1080/00288306.2015.1076862>
- 370 Boisson, J.-Y., Bertrand, L., Heitz, J.-F., & Golvan, Y. (2001). In situ and laboratory
371 investigations of fluid flow through an argillaceous formation at different scales of space
372 and time, Tournemire tunnel, southern France. *Hydrogeology Journal*, 9(1), 108–123.
373 <https://doi.org/10.1007/s100400000119>
- 374 Boulton, C., Niemeijer, A. R., Hollis, C. J., Townend, J., Raven, M. D., Kulhanek, D. K., &
375 Shepherd, C. L. (2019). Temperature-dependent frictional properties of heterogeneous
376 Hikurangi Subduction Zone input sediments, ODP Site 1124. *Tectonophysics*, 757, 123–
377 139. <https://doi.org/10.1016/j.tecto.2019.02.006>
- 378 Boulton, C., Mizera, M., Niemeijer, A. R., Little, T. A., Müller, I. A., Ziegler, M., & Hamers, M.
379 F. (2022). Observational and theoretical evidence for frictional-viscous flow at shallow
380 crustal levels. *Lithos*, 428–429, 106831. <https://doi.org/10.1016/j.lithos.2022.106831>
- 381 Burgreen-Chan, B., Meisling, K. E., & Graham, S. (2016). Basin and petroleum system
382 modelling of the East Coast Basin, New Zealand: a test of overpressure scenarios in a
383 convergent margin. *Basin Research*, 28(4), 536–567. <https://doi.org/10.1111/bre.12121>
- 384 Carman, P. C. (1997). Fluid flow through granular beds. *Chemical Engineering Research and*
385 *Design*, 75, S32–S48. [https://doi.org/10.1016/S0263-8762\(97\)80003-2](https://doi.org/10.1016/S0263-8762(97)80003-2)
- 386 Dutilleul, J., Bourlange, S., & Géraud, Y. (2021). Porosity and compaction state at the active
387 Pāpaku thrust fault in the frontal accretionary wedge of the north Hikurangi margin. *G3*,
388 22, e2020GC009325. <https://doi.org/10.1029/2020GC009325>

- 389 Dvorkin, J., & Nur, A. (1996). Elasticity of high-porosity sandstones: Theory for two North Sea
390 data sets. *GEOPHYSICS*, *61*(5), 1363–1370. <https://doi.org/10.1190/1.1444059>
- 391 Eberhart-Phillips, D., Han, D.-H., & Zoback, M. D. (1989). Empirical relationships among
392 seismic velocity, effective pressure, porosity, and clay content in sandstone.
393 *GEOPHYSICS*, *54*(1), 82–89. <https://doi.org/10.1190/1.1442580>
- 394 Ellis, S., Fagereng, Å., Barker, D., Henrys, S., Saffer, D., Wallace, L., et al. (2015). Fluid
395 budgets along the northern Hikurangi subduction margin, New Zealand: the effect of a
396 subducting seamount on fluid pressure. *GJI*, *202*, 277–297.
397 <https://doi.org/10.1093/gji/ggv127>
- 398 Fagereng, Å., Savage, H. M., Morgan, J. K., Wang, M., Meneghini, F., Barnes, P. M., et al.
399 (2019). Mixed deformation styles observed on a shallow subduction thrust, Hikurangi
400 margin, New Zealand. *Geology*, *47*, 872–876. <https://doi.org/10.1130/G46367.1>
- 401 Freed, R. L., & Peacor, D. R. (1989). Variability in temperature of the smectite/illite reaction in
402 Gulf Coast sediments. *Clay Minerals*, *24*(2), 171–180.
403 <https://doi.org/10.1180/claymin.1989.024.2.05>
- 404 French, M. E., & Morgan, J. K. (2020). Pore Fluid Pressures and Strength Contrasts Maintain
405 Frontal Fault Activity, Northern Hikurangi Margin, New Zealand. *GRL*, *47*,
406 e2020GL089209. <https://doi.org/10.1029/2020GL089209>
- 407 Gase, A. C., Van Avendonk, H. J. A., Bangs, N. L., Bassett, D., Henrys, S. A., Barker, D. H. N.,
408 et al. (2021). Crustal Structure of the Northern Hikurangi Margin, New Zealand: Variable
409 Accretion and Overthrusting Plate Strength Influenced by Rough Subduction. *Journal of*
410 *Geophysical Research: Solid Earth*, *126*(5), e2020JB021176.
411 <https://doi.org/10.1029/2020JB021176>

- 412 Gassmann, F. (1951). Elastic waves through a packing of spheres. *GEOPHYSICS*, 16(4), 673–
413 685. <https://doi.org/10.1190/1.1437718>
- 414 Griffiths, F. J., & Joshi, R. C. (1989). Change in pore size distribution due to consolidation of
415 clays. *Géotechnique*, 39(1), 159–167. <https://doi.org/10.1680/geot.1989.39.1.159>
- 416 Hunt, J. M. (1996). *Petroleum geochemistry and geology* (2nd ed). New York: W.H. Freeman.
- 417 Im, K., Saffer, D., Marone, C., & Avouac, J. P. (2020). Slip-rate-dependent friction as a
418 universal mechanism for slow slip events. *Nature Geoscience*, 13(10).
419 <https://doi.org/10.1038/s41561-020-0627-9>
- 420 Intera Eng. Ltd. (2011). *Descriptive Geosphere Site Model*. 2011: Intera Eng. Ltd.
- 421 Kitajima, H., & Saffer, D. M. (2012). Elevated pore pressure and anomalously low stress in
422 regions of low frequency earthquakes along the Nankai Trough subduction megathrust:
423 LOW STRESS AT LOW SEISMIC VELOCITY ZONE. *Geophysical Research Letters*,
424 39(23), n/a-n/a. <https://doi.org/10.1029/2012GL053793>
- 425 Kobayashi, T., & Sato, T. (2021). Estimating Effective Normal Stress During Slow Slip Events
426 From Slip Velocities and Shear Stress Variations. *Geophysical Research Letters*, 48(20).
427 <https://doi.org/10.1029/2021GL095690>
- 428 Kodaira, S., Iidaka, T., Kato, A., Park, J.-O., Iwasaki, T., & Kaneda, Y. (2004). High pore fluid
429 pressure may cause silent slip in the Nankai Trough. *Science*, 304, 1295–1298.
- 430 van de Lagemaat, S. H. A., Mering, J. A., & Kamp, P. J. J. (2022). Geochemistry of syntectonic
431 carbonate veins within Late Cretaceous turbidites, Hikurangi margin (New Zealand):
432 Implications for a mid-Oligocene age of subduction initiation. *G3*, 23, e2021GC010125.
433 <https://doi.org/10.1029/2021GC010125>

- 434 Leah, H., Fagereng, Å., Bastow, I., Bell, R., Lane, V., Henrys, S., et al. (2022). The northern
435 Hikurangi margin three-dimensional plate interface in New Zealand remains rough 100
436 km from the trench. *Geology*, *50*, 1256–1260. <https://doi.org/10.1130/G50272.1>
- 437 Liu, H.-P., Anderson, D. L., & Kanamori, H. (1976). Velocity dispersion due to anelasticity;
438 implications for seismology and mantle composition. *Geophysical Journal International*,
439 *47*(1), 41–58. <https://doi.org/10.1111/j.1365-246X.1976.tb01261.x>
- 440 Magara, K. (1978). *Compaction and fluid migration: practical petroleum geology*. Amsterdam,
441 New York: Elsevier Scientific Pub. Co. ; Distributors for the U.S. and Can., Elsevier
442 North-Holland.
- 443 Mazengarb, C., & Speden, I. G. (2000). Geology of the Raukumara area. geological map 6 60 p.
444 + 1 fold. map, Lower Hutt: Institute of Geological & Nuclear Sciences.
- 445 Mondol, N. H., Bjørlykke, K., & Jahren, J. (2008). Experimental compaction of clays:
446 relationship between permeability and petrophysical properties in mudstones. *Petroleum*
447 *Geoscience*, *14*(4), 319–337. <https://doi.org/10.1144/1354-079308-773>
- 448 Morgan, J. K., Solomon, E. A., Fagereng, A., Savage, H. M., Wang, M., Meneghini, F., et al.
449 (2022). Seafloor overthrusting causes ductile fault deformation and fault sealing along the
450 Northern Hikurangi Margin. *Earth and Planetary Science Letters*, *593*, 117651.
451 <https://doi.org/10.1016/j.epsl.2022.117651>
- 452 Mortimer, N., Rattenbury, M., King, P., Bland, K., Barrell, D., Bache, F., et al. (2014). High-
453 level stratigraphic scheme for New Zealand rocks. *New Zealand Journal of Geology and*
454 *Geophysics*, *57*(4), 402–419. <https://doi.org/10.1080/00288306.2014.946062>
- 455 Neglia, S. (1979). Migration of Fluids in Sedimentary Basins¹. *AAPG Bulletin*, *63*(4), 573–597.
456 <https://doi.org/10.1306/2F918194-16CE-11D7-8645000102C1865D>

- 457 Neuzil, C. E. (1994). How permeable are clays and shales? *Water Resources Research*, 30(2),
458 145–150. <https://doi.org/10.1029/93WR02930>
- 459 Neuzil, C. E. (2019). Permeability of Clays and Shales. *Annual Review of Earth and Planetary*
460 *Sciences*, 47(1), 247–273. <https://doi.org/10.1146/annurev-earth-053018-060437>
- 461 Passarelli, L., Selvadurai, P. A., Rivalta, E., & Jónsson, S. (2021). The source scaling and
462 seismic productivity of slow slip transients. *Science Advances*, 7(32), eabg9718.
463 <https://doi.org/10.1126/sciadv.abg9718>
- 464 Pecher, I. A., Villinger, H., Kaul, N., Crutchley, G. J., Mountjoy, J. J., Huhn, K., et al. (2017). A
465 Fluid Pulse on the Hikurangi Subduction Margin: Evidence From a Heat Flux Transect
466 Across the Upper Limit of Gas Hydrate Stability. *Geophysical Research Letters*, 44(24).
467 <https://doi.org/10.1002/2017GL076368>
- 468 Rabinowitz, H. S., Savage, H. M., Skarbek, R. M., Ikari, M. J., Carpenter, B. M., & Collettini, C.
469 (2018). Frictional behavior of input sediments to the Hikurangi trench, New Zealand. *G3*,
470 19, 2973–2990. <https://doi.org/10.1029/2018GC007633>
- 471 Reece, J. S., Flemings, P. B., Dugan, B., Long, H., & Germaine, J. T. (2012). Permeability-
472 porosity relationships of shallow mudstones in the Ursa Basin, northern deepwater Gulf
473 of Mexico: MUDSTONE PERMEABILITY-POROSITY BEHAVIOR. *Journal of*
474 *Geophysical Research: Solid Earth*, 117(B12), n/a-n/a.
475 <https://doi.org/10.1029/2012JB009438>
- 476 Reisdorf, A. G., Hostettler, B., Jaeggi, D., Deplazes, G., Blaesi, H., Morard, A., et al. (2016).
477 Litho- and biostratigraphy of the 250 m-deep Mont Terri BDB-1 borehole through the
478 Opalinus Clay and bounding formations, St Ursanne, Switzerland.
479 <https://doi.org/10.13140/RG.2.2.15045.04322>

- 480 Roberts, R., Chace, D., Beauheim, R., & Avis, J. (2011). *Analysis of straddle-packer tests in*
481 *DGR boreholes* (Technical report No. TR-08-32). Ottawa, Canada: Geofirma Eng. Ltd.
- 482 Saffer, D. M., & Bekins, B. A. (1998). Episodic fluid flow in the Nankai accretionary complex:
483 Timescale, geochemistry, flow rates, and fluid budget. *Journal of Geophysical Research:*
484 *Solid Earth*, 103(B12), 30351–30370. <https://doi.org/10.1029/98JB01983>
- 485 Saffer, D. M., & Wallace, L. M. (2015). The frictional, hydrologic, metamorphic and thermal
486 habitat of shallow slow earthquakes. *NG*, 8, 594–600. <https://doi.org/10.1038/ngeo2490>
- 487 Saxena, N., & Mavko, G. (2014). Exact equations for fluid and solid substitution.
488 *GEOPHYSICS*, 79(3), L21–L32. <https://doi.org/10.1190/geo2013-0187.1>
- 489 Schwartz, S. Y., & Rokosky, J. M. (2007). Slow slip events and seismic tremor at circum-Pacific
490 subduction zones. *RG*, 45, RG3004. <https://doi.org/10.1029/2006RG000208>
- 491 Shaddock, H. R., & Schwartz, S. Y. (2019). Subducted seamount diverts shallow slow slip to the
492 forearc of the northern Hikurangi subduction zone, New Zealand. *Geology*, 47, 415–418.
493 <https://doi.org/10.1130/G45810.1>
- 494 Shreedharan, S., Ikari, M., Wood, C., Saffer, D., Wallace, L., & Marone, C. (2022). Frictional
495 and Lithological Controls on Shallow Slow Slip at the Northern Hikurangi Margin. *G3*,
496 23, e2021GC010107. <https://doi.org/10.1029/2021GC010107>
- 497 Shreedharan, S., Saffer, D., Wallace, L. M., & Williams, C. (2023). Ultralow frictional healing
498 explains recurring slow slip events. *Science*, 379(6633), 712–717.
499 <https://doi.org/10.1126/science.adf4930>
- 500 Skempton, A. W. (1969). The consolidation of clays by gravitational compaction. *Quarterly*
501 *Journal of the Geological Society*, 125(1–4), 373–411.
502 <https://doi.org/10.1144/gsjgs.125.1.0373>

- 503 Sun, T., Saffer, D., & Ellis, S. (2020). Mechanical and hydrological effects of seamount
504 subduction on megathrust stress and slip. *Nature Geoscience*, *13*(3), 249–255.
505 <https://doi.org/10.1038/s41561-020-0542-0>
- 506 Sutherland, H. J., & Cave, S. P. (1980). Argon gas permeability of new mexico rock salt under
507 hydrostatic compression. *International Journal of Rock Mechanics and Mining Sciences*
508 *& Geomechanics Abstracts*, *17*(5), 281–288. [https://doi.org/10.1016/0148-](https://doi.org/10.1016/0148-9062(80)90810-4)
509 [9062\(80\)90810-4](https://doi.org/10.1016/0148-9062(80)90810-4)
- 510 Tisato, N., & Marelli, S. (2013). Laboratory measurements of the longitudinal and transverse
511 wave velocities of compacted bentonite as a function of water content, temperature, and
512 confining pressure: ELASTIC PROPERTIES OF BENTONITE. *Journal of Geophysical*
513 *Research: Solid Earth*, *118*(7), 3380–3393. <https://doi.org/10.1002/jgrb.50252>
- 514 Tisato, N., Madonna, C., & Saenger, E. H. (2021). Attenuation of Seismic Waves in Partially
515 Saturated Berea Sandstone as a Function of Frequency and Confining Pressure. *Frontiers*
516 *in Earth Science*, *9*, 641177. <https://doi.org/10.3389/feart.2021.641177>
- 517 Tsuji, T., & Iturrino, G. J. (2008). Velocity-porosity relationships in oceanic basalt from eastern
518 flank of the Juan de Fuca Ridge: The effect of crack closure on seismic velocity.
519 *Exploration Geophysics*, *39*(1), 41–51. <https://doi.org/10.1071/EG08001>
- 520 Tsuji, T., Tokuyama, H., Costa Pisani, P., & Moore, G. (2008). Effective stress and pore pressure
521 in the Nankai accretionary prism off the Muroto Peninsula, southwestern Japan. *Journal*
522 *of Geophysical Research*, *113*(B11), B11401. <https://doi.org/10.1029/2007JB005002>
- 523 Villar, M. V., Martín, P. L., & Barcala, J. M. (2005). Modification of physical, mechanical and
524 hydraulic properties of bentonite by thermo-hydraulic gradients. *Engineering Geology*,
525 *81*(3), 284–297. <https://doi.org/10.1016/j.enggeo.2005.06.012>

- 526 Vora, H. B., & Dugan, B. (2019). Porosity-Permeability Relationships in Mudstone from Pore-
527 Scale Fluid Flow Simulations using the Lattice Boltzmann Method. *Water Resources*
528 *Research*, 55(8), 7060–7071. <https://doi.org/10.1029/2019WR024985>
- 529 Wallace, Laura M. (2020). Slow Slip Events in New Zealand. *AREPS*, 48, 175–203.
530 <https://doi.org/10.1146/annurev-earth-0717190055104>
- 531 Wallace, L.M., Saffer, D. M., Barnes, P. M., Pecher, I. A., Petronotis, K. E., LeVay, L. J., & the
532 Expedition 372/375 Scientists. (2019). *Hikurangi Subduction Margin Coring, Logging,*
533 *and Observatories*. College Station, TX: Proceedings of the International Ocean
534 Discovery Program, 372B/375. <https://doi.org/10.14379/iodp.proc.372B375.102.2019>
- 535 Walsh, R. (2011). *Compilation and consolidation of field and laboratory data for*
536 *hydrogeological properties* (DGR Site Charact. Doc. No. TR-08-10). Ottawa, Canada:
537 Geofirma Eng. Ltd.
- 538 Warren-Smith, E., Fry, B., Wallace, L., Chon, E., Henrys, S., Sheehan, A., et al. (2019). Episodic
539 stress and fluid pressure cycling in subducting oceanic crust during slow slip. *Nature*
540 *Geoscience*, 12(6), 475–481. <https://doi.org/10.1038/s41561-019-0367-x>
- 541 Yohler, R., Bartlow, N., Wallace, L. M., & Williams, C. (2019). Time-Dependent Behavior of a
542 Near-Trench Slow-Slip Event at the Hikurangi Subduction Zone. *Geochemistry,*
543 *Geophysics, Geosystems*, 20(8), 4292–4304. <https://doi.org/10.1029/2019GC008229>
- 544 Yu, C., Matray, J.-M., Gonçalves, J., Jaeggi, D., Gräsle, W., Wiczorek, K., et al. (2017).
545 Comparative study of methods to estimate hydraulic parameters in the hydraulically
546 undisturbed Opalinus Clay (Switzerland). *Swiss Journal of Geosciences*, 110(1), 85–104.
547 <https://doi.org/10.1007/s00015-016-0257-9>
- 548

1 **Permeability and elastic properties of rocks from the northern Hikurangi margin:**
2 **Implications for slow-slip events**

3 **Nicola Tisato¹, Carolyn D. Bland^{1*}, Harm Van Avendonk², Nathan Bangs², Hector Garza¹,**
4 **Omar Alamoudi¹, Kelly Olsen^{2†}, Andrew Gase^{2‡}**

5 ¹ Department of Earth and Planetary Sciences, Jackson School of Geosciences, The University of
6 Texas at Austin, Austin, TX, U.S.

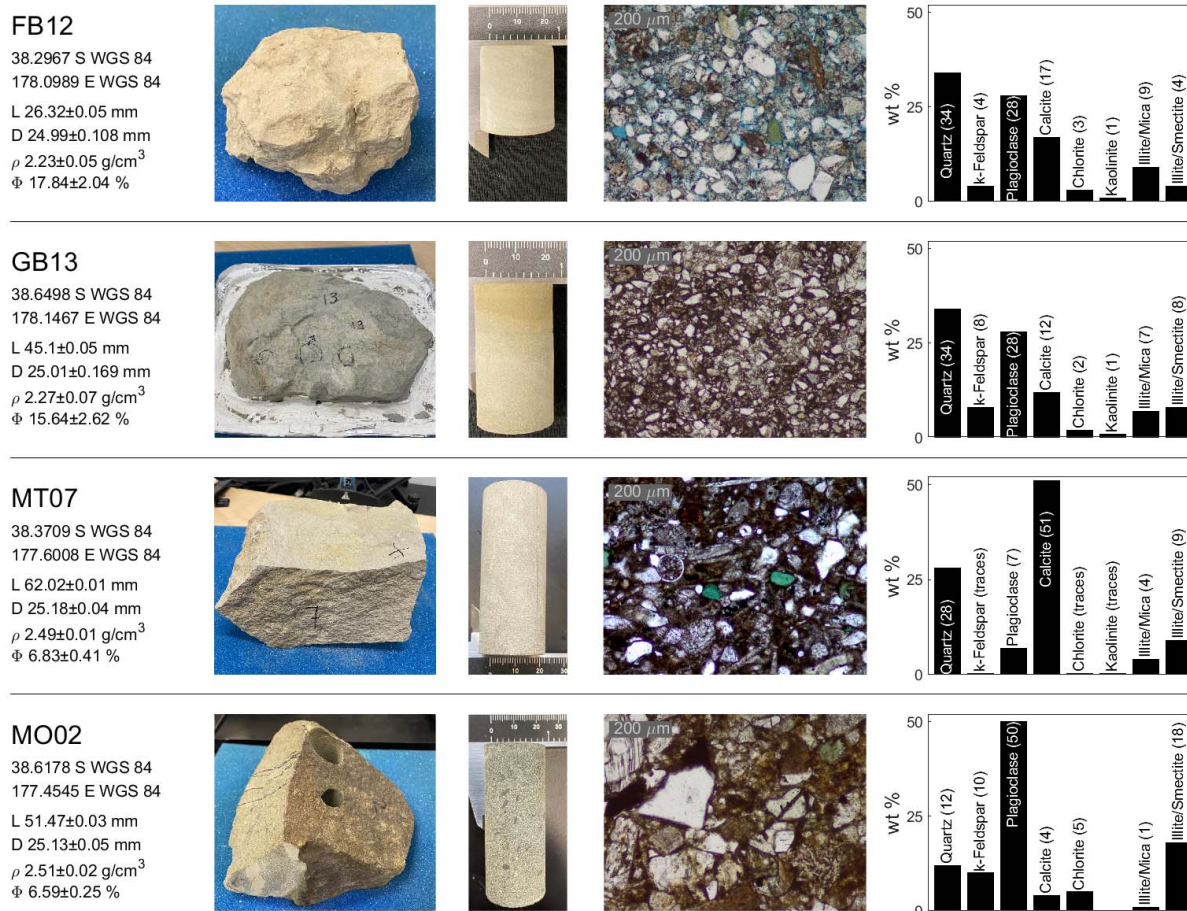
7 ³ Institute for Geophysics, Jackson School of Geosciences, The University of Texas at Austin,
8 Austin, TX, U.S.

9 * Now at: Pariveda Solutions, Dallas, TX, U.S.

10 † Now at: Descartes Labs, 1607 Paseo de Peralta, Suite B, Sante Fe, NM, U.S.

11 ‡ Now at: Geology Department, Western Washington University, Bellingham, WA, U.S.

12
13 Corresponding author: Nicola Tisato (nicola.tisato@jsg.utexas.edu)
14



15 **Figure S1.** For each sample, the left column reports the geographic coordinates, length (L),
 16 **diagonal (D), density (ρ), and porosity (Φ).** The three center columns are pictures of hand
 17 **samples and transmitted light microphotographs.** The right column reports mineral
 18 **compositions according to X-ray diffraction analyses (XRD).**

19
 20 **Sample preparation details**

21 The end faces of each core plug were smoothed to parallel using a rock saw and a lathe
 22 equipped with an angular grinder. Parallelism was checked with a 0.01 mm resolution caliper.
 23 Each core was oven-dried at ~333 K for several days to reduce absorbed water. We then
 24 calculated the total volume and density of each core by measuring its mass and dimensions using
 25 a scale and a caliper to accuracies of 0.001 g and 0.02 mm, respectively. A helium pycnometer
 26 (Micromeritics AccuPyc II 1340) was used to measure the solid volume and porosity of each
 27 core.

28 To evenly distribute the saturating water or the helium gas to test permeability across the
 29 sample end-face, we placed 3.175 mm thickness, 10 μ m grain size, AISI 316 stainless steel
 30 porous frits between each sample holder and the adjacent sample end-face.

31 Sample MT07 at stage S3 - i.e., fractured after being exposed to humidity - was epoxy
 32 impregnated before removing the rubber jacket to avoid offsetting the fracture.

33

34 Preparation of the saturating water for sample GB13

35 Water chemically equilibrated with sample GB13 was prepared and injected as follows:
36 For several weeks before saturation, we submerged a few grams of GB13 granules in deionized
37 water. Then, the injection of such aqueous fluid was performed using a high-pressure syringe
38 pump (ISCO 260HP), recording – via a Matlab script - the injected volume and injection
39 pressure. The latter was maintained constant to a value of 3 MPa lower than the confining
40 pressure that varied between 20 and 50 MPa.

41

42 Ultrasonic and mechanical testing details

43 Our samples have a maximum ultrasonic velocity of ~6 km/s and considering the testing
44 frequency of 800 kHz, we estimated a maximum wavelength (λ_M) of 7.5 mm and, to avoid
45 nearfield effects, we prepared cores with a length (L) > 3 λ_M . Velocities were estimated with the
46 transmission method by measuring the time of travel of the elastic wave along the core plug
47 (Birch, 1960). We corrected the first arrival by the delay introduced by the sample holders that
48 was determined by a standard calibration procedure (e.g., Prelicz, 2005). A pulser-receiver
49 apparatus (JSR Ultrasonics DPR300) generated a negative spike pulse with a typical duration of
50 ~40 ns feeding the source ultrasonic transducer. We used a pulsing rate of 100 pulses/sec (PRF
51 RATE=1), pulse amplitude of ~194 V (PULSE AMPLITUDE = 4, and PULSE ENERGY =
52 HIGH Z 4), and damping of 331 Ohms (DAMPING = 1). In addition, the pulser-receiver
53 produces a trigger signal (5 V in amplitude) to synchronize the pulser and the oscilloscope (Rigol
54 DS1104Z-S) collecting the signals generated by the receiving transducer and amplified by the
55 receiver. The latter has a gain of 66 dB (REL. GAIN = 79), a high-pass filter corner frequency of
56 1 MHz, and a low-pass filter corner frequency of 3 MHz. Two data transfer switches allow
57 selecting the recording of the V_P , V_{S1} or V_{S2} signal. To improve the signal-to-noise ratio the
58 oscilloscope collects and stacks 1024 signals and transmits the digitized wavelets to a computer
59 via a USB port. Typically, the signal, comprising 1200 samples, is digitized every 0.2 μ s or less
60 and saved as a comma-separated-value (CSV) file. Shear velocities were calculated as the
61 average of V_{S1} and V_{S2} .

62 All velocities (V) as a function of σ_M were fit according to Eberhart-Phillips et al., 1989:

$$63 \quad V = a + k \sigma_M - b e^{-d \sigma_M} \quad \text{eq. S1}$$

64 Where a , k , b , and d are fitting parameters. Table S1 reports the fitting parameters for all the
65 measurements reported in Figure 2A. As σ_M increases, especially above ~50 MPa, the effect of
66 the non-linear part of eq. S1 decreases, and V tends to be equal to:

$$67 \quad V = a + k \sigma_M \quad \text{eq. S2}$$

68 The exponential increase of velocity (e.g., $-b e^{-d \sigma_M}$) is controlled by crack closure (e.g.,
69 Eberhart-Phillips et al., 1989; Tsuji & Iturrino, 2008). Cracks are naturally occurring, but some
70 of our sample cracks were probably produced during preparation. Therefore, the measured
71 velocities and those modeled with eq. S1 possibly underestimate the velocities of the undisturbed
72 rocks. On the other end, the velocities calculated according to eq. S2 represent an upper bound
73 for the undisturbed rock velocities. Therefore, to provide a range of possible velocities, table S2
74 reports values calculated according to eqs. S1 and S2, and we used their average to color code
75 the symbols in Figure 4B, which compares ultrasonic and seismic velocities in section MC10
76 (fig. 4A).

77 We estimated the ultrasonic wave velocities of the saturated sample GB13 (wet) using the
78 Gassmann fluid substitution (Gassmann, 1951). We obtained the dry bulk and shear modulus
79 from the measured ultrasonic velocities and density. We used a porosity of 15.64% and estimated

80 the effective bulk modulus of the mineral material making up the rock ($K_0=41.9$ GPa) using the
 81 Voigt-Reuss-Hill average (Hill, 1952). Such an average was calculated considering the mineral
 82 abundances and bulk moduli in Table S3.

83 Samples compaction was measured to 1 μm accuracy with a Linear Variable
 84 Displacement Transducer connected to the axial piston, whose signal was acquired along with
 85 the confining pressure and vertical force.

86

Sample	Vp a, km/s	Vp k, km/(s MPa)	Vp b, km/s	Vp d, 1/MPa	Vs a, km/s	Vs k, km/(s MPa)	Vs b, km/s	Vs d, 1/MPa
MT07	4.259	0.00040	0.5508	0.01559	2.287	0.00040	0.0979	0.0403
MO02	4.833	0.00048	0.9625	0.01998	2.671	0.00107	0.3333	0.0469
FB12	3.411	0.00149	0.8080	0.01892	1.935	0.00052	0.6075	0.0280
FB12 compacted	3.655	0.00221	0.6489	0.01697	2.087	0.00048	0.5253	0.0135
GB13 dry	3.198	0.00040	0.6979	0.05500	1.925	0.00040	0.3755	0.0530
GB13 wet	3.120	0.00453	0.4441	0.30994	1.598	0.00370	0.0215	0.0301

87 **Table S1: Fitting parameters for the samples ultrasonic velocities according to eqs. S1 and**
 88 **S2.**

89

Sample	Φ , %	κ , m ²	σ_M , MPa	Vp (meas.) km/s	Vp (EP89) min, km/s	Vp (EP89) max, km/s	Vp (EP89) mean, km/s
FB12	17.3	3.95E-16	10	2.788	2.757	3.426	3.092
FB12	16.0	3.52E-16	20	2.937	2.887	3.441	3.164
FB12	15.6	3.04E-16	30	2.986	2.998	3.456	3.227
FB12	13.7	1.63E-16	50	3.055	3.172	3.486	3.329
FB12	13.4	1.24E-16	70	3.251	3.301	3.515	3.408
FB12	14.1	2.60E-16	30	2.968	2.998	3.456	3.227
FB12	14.4	3.38E-16	20	2.895	2.887	3.441	3.164
FB12 compacted	14.0	2.13E-17	30	3.333	3.331	3.721	3.526
FB12 compacted	14.0	1.46E-17	70	3.543	3.611	3.809	3.710
FB12 compacted	11.7	5.97E-18	150	3.866	3.935	3.986	3.961
FB12 compacted	10.3	3.64E-18	200	4.008	4.075	4.097	4.086
FB12 compacted	10.3	5.10E-18	150	3.863	3.935	3.986	3.961
FB12 compacted	10.4	5.56E-18	100	3.745	3.757	3.876	3.816
FB12 compacted	10.4	8.67E-18	70	3.618	3.611	3.809	3.710
FB12 compacted	11.2	1.54E-17	30	3.298	3.331	3.721	3.526
MO02	5.9	8.47E-20	30	4.353	4.320	4.848	4.584
MO02	5.5	7.80E-21	50	4.479	4.502	4.857	4.680
MT07	6.4	2.03E-20	30	3.838	3.926	4.271	4.098
MT07	6.2	1.39E-20	50	3.913	4.026	4.279	4.153
MT07	6.0	6.29E-21	70	3.995	4.102	4.287	4.194
MT07	6.4	1.92E-20	20	3.843	3.864	4.267	4.065

90 **Table S2: Porosity, permeability, mean stress, and Vp for our sample data that are**
 91 **reported in Figure 4B. ‘Vp (meas.)’ indicate the measurements, ‘Vp (EP89) min’ is the**
 92 **velocity estimated using eq. S1, ‘Vp (EP89) max’ is the velocity estimated according to eq.**
 93 **S2. ‘Vp (EP89) mean’ is the average between ‘Vp (EP89) min’ and ‘Vp (EP89) max’. The**
 94 **latter is used to color-code the symbols of samples MT07, MO02, and FB12 in Figure 4B.**

95

96

Mineral	Fraction	Bulk Modulus
Quartz	34%	37.0 GPa
K-feldspar	8%	37.5 GPa
Plagioclase	28%	76.0 GPa
Calcite	12%	77.0 GPa
Clays	18%	15.0 GPa

98 **Table S3. Parameters used to calculate the effective bulk modulus of the minerals making**
 99 **up sample GB13 (K_0). Fractions are estimated from XRD (see Figure S1), and bulk moduli**
 100 **are taken from (Carmichael, 1989).**

101

102 Permeability testing

103 The two reservoirs connected to the sample end-faces have volumes $V_1=58.725$ ml and
 104 $V_2=162.53$ ml, and at the beginning of the test, we connected the reservoirs to a high-pressure
 105 helium gas bottle to raise their internal pressures to two different values $P_{1i} > P_{2i}$. While P_{1i} is
 106 greater than P_{2i} , helium flows through the sample until pressure equilibrium is reached. Two
 107 digital manometers (Keller LEO3) connected to a computer and a Matlab code record P1 and P2
 108 over time (t). The two manometers also measure temperature (T). Permeability is then calculated
 109 as:

$$110 \quad \kappa = -\frac{\beta \eta L}{\left(\frac{1}{V_1} + \frac{1}{V_2}\right) K A}, \quad \text{eq. S3}$$

111 Where η and K are Helium viscosity and bulk modulus, respectively; L and A are the lengths
 112 and cross-section area of the sample; β is the exponent of the pressure decay:

$$113 \quad P_1 = (P_{1i} - P_{2i}) e^{\beta t} + P_f, \quad \text{eq. S4}$$

114 Where P_f is the equilibrium pressure, i.e., P_1 and P_2 at time infinite. We assume helium
 115 properties as a function of pressure and temperature from the national institute for standards and
 116 technology (NIST) fluid thermophysical properties (Arp et al., 1998; Ortiz-Vega et al., 2020). P_f
 117 and β were estimated by means of a non-linear least absolute residuals fit implemented in
 118 Matlab.

119

120 XRD and CT-scanner setup

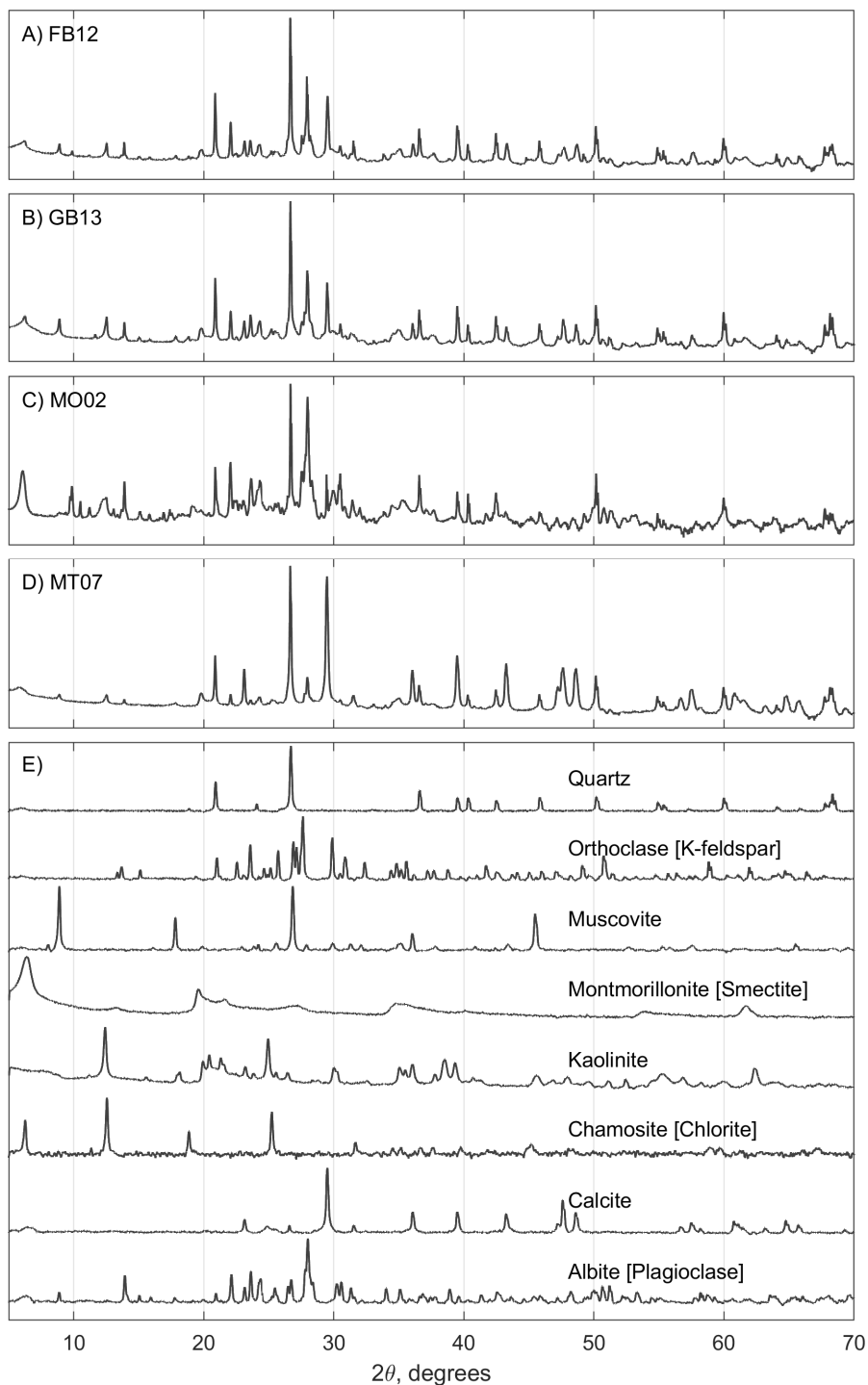
121 Mineralogical X-ray diffraction analyses were conducted at the Geomaterials
 122 Characterization and Imaging Facility (GeoMatCI) at The University of Texas at Austin. Whole
 123 rock samples were manually homogenized, ground, and sieved to a 250 μm mesh size. XRD
 124 analyses were performed using a Bruker D8 diffractometer instrument equipped with $\text{Cu K}\alpha$
 125 radiation and a nickel filter, along with a LYNXEYE solid-state detector. The analyses were
 126 carried out at a voltage of 45 kV and a current of 40 mA, employing a 2θ scan axis ranging from
 127 3° to 70° , with step increments of $.0195^\circ$ (2θ) and a duration of 1 s per step. Whole rock X-ray
 128 patterns (Fig S2) were determined through Rietveld refinement utilizing Bruker TOPAS 4.2
 129 software.

130 For clay speciation analyses (Fig S3), we followed the modified methods based on Hillier
 131 (2000) and Moore & Reynolds (1997). CaCO_3 rich samples were subjected to a modified HCl-
 132 Na_2CO_2 treatment (5% diluted HCl) to disseminate clay minerals following the method of
 133 Komadel et al. (1990) and Meredith E. Ostrom (1961). Disaggregated material was separated
 134 into a <2-micron clay fraction suspension using sodium hexametaphosphate, enabling the

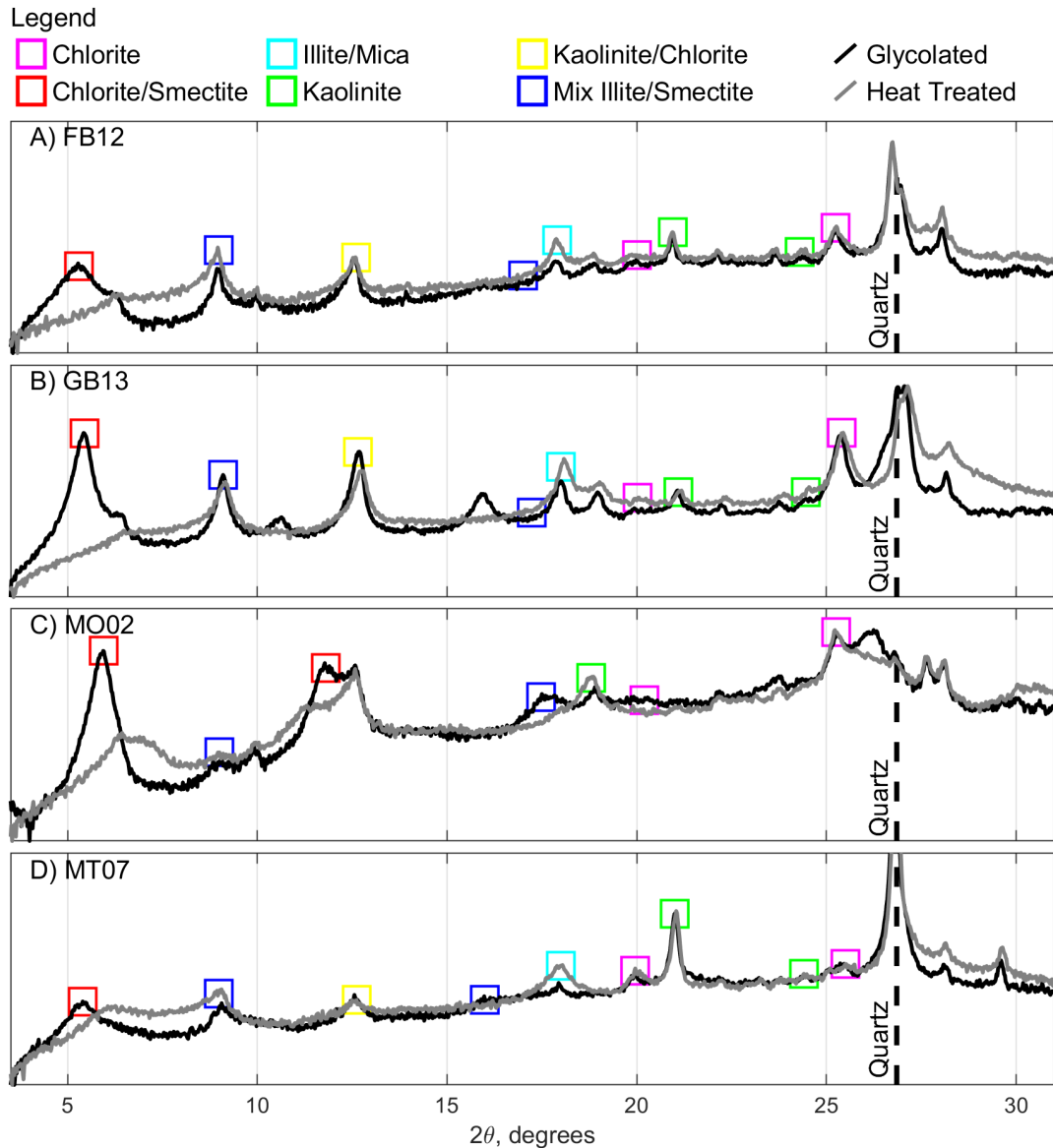
135 acquisition of clay speciation by excluding heavier non-phyllosilicate minerals. The <2-micron
136 clay suspension was vacuum-filtered through a millipore filter and subsequently oriented onto a
137 glass slide. The oriented clay mounts were subjected to ethylene glycol vapors for 24 hours,
138 followed by heating (1 hour) to 400°C to identify swelling clays. Clay speciation X-ray patterns
139 with a 2θ scan axis ranging from 3° to 70°, with step increments of 0.195° (2θ) and a duration of
140 1 s per step were evaluated using reference intensity ratios (RIR), and mineral intensity factors
141 (MIF) with the MDI Jade software.

142 For CT-scanning we used an NSI scanner equipped with a Fein Focus High Power
143 source, at 120 kV voltage and 0.14 mA current. CT scans were acquired at 33.3 μm per voxel
144 resolution. The X-ray source was filtered using aluminum foil. The CT scanner is equipped with
145 a Perkin Elmer detector, with 0.5 pF gain, and the 1800 projections were collected at 1 fps and
146 1x1 binning. The source-to-object distance was 150.566 mm, and the source to detector 963.799
147 mm. We performed a continuous CT scan by averaging 2 frames and by skipping 0 frames. We
148 applied a beam-hardening correction of 0.25 and a post-reconstruction ring correction using the
149 following parameters: oversample = 2, radial bin width = 21, sectors = 32, minimum arc length =
150 2, angular bin width = 9, angular screening factor = 4. The final reconstructed volume had a
151 voxel size of 33.3 μm and 1873 slices.

152



153
 154 **Figure S2. A-D) XRD spectra of the four samples. E) Standard spectra for the mineral**
 155 **comprising our samples. Data have been taken from the RRUFF database (Lafuente et al.,**
 156 **2015): Talc URL=rruff.info/R040137; Quartz URL=rruff.info/R040031; Orthoclase**
 157 **URL=rruff.info/R040055; Muscovite URL=rruff.info/R040104; Montmorillonite**
 158 **URL=rruff.info/R110052; Kaolinite URL=rruff.info/R140004; Chamosite**
 159 **URL=rruff.info/R060188; Calcite URL=rruff.info/R040070; Albite**
 160 **URL=rruff.info/R040068.**



161
 162 **Figure S3.** XRD clay patterns (oriented, glycolated, heat-treated at 400°C) for Illite/Mica, Mix
 163 Illite/Smectite, Kaolinite, and Chlorite minerals. Squares indicate peaks and portions of spectra
 164 used to speciate and estimate clay fractions for each sample.

165 A) Sample FB12 is dominated by Illite/Mica, followed by Mix Illite/Smectite, with minor
 166 quantities of Chlorite and Kaolinite. B) Sample GB13 exhibits an abundance of Mix
 167 Illite/Smectite and Illite/Mica, along with trace amounts of Chlorite and Kaolinite. C) Sample
 168 MO02 is notably rich in Mix Illite/Smectite, with a significant presence of Chlorite and minor
 169 content of Illite/Mica.

170 D) Sample MT07 is primarily rich in Mix Illite/Smectite, featuring a notable abundance of
 171 Illite/Mica, and minor quantities of Chlorite and Kaolinite.

172
 173

174 Fracture aperture calculation

175 To normalize CT-scan datasets, we fit a Gaussian function to the distribution of CT
 176 numbers to obtain a CT-number mean (m_x) and standard deviation (s_x), where x is either S1, S2,

177 or S3. To compare datasets acquired at different stages, we shifted the CT-numbers of datasets
178 S2 and S3 by $m_{S1}-m_{S2}$ and $m_{S1}-m_{S3}$, respectively. We added a value of 1 to each voxel, cropped
179 each image to 718x718 pixels around the sample center, and assigned a value of 0 to pixels with
180 a distance $>718/2$ from the sample center. We binarized the datasets to assign each voxel to
181 either solid rock or air by applying a threshold calculated as:

$$182 \quad t_x = m_x - 2.5 s_x \quad \text{eq. S5}$$

183 Voxels with CT-number equal to or greater than t_x were assumed to represent rock and
184 assigned a value of 255. Voxels with CT-number lower than t_x and greater than zero were
185 assumed to be air and assigned a value of 128.

186 To obtain a FADP of a binarized dataset, we calculated: 1) The Euclidian distance of
187 each voxel in the fracture. This is achieved by a) performing an iterative image morphological
188 erosion assigning approximated distances of each fracture voxel from the fracture rim, and b)
189 calculating the Euclidian distance of each voxel within the fracture from the closest voxel
190 representing rock; 2) The skeleton of the fracture (SK) comprises the voxels that are within the
191 fracture and have the maximum Euclidian distance from the fracture rim into respect the 26
192 surrounding voxels. Such a device extracts the center surface while preserving the topology and
193 Euler number, also known as the Euler characteristic of the objects (Kerschnitzki et al., 2013;
194 Lee et al., 1994). Finally, the FADP was calculated at each SK location by doubling the
195 Euclidian distance recorded in such voxels.

196

197 **References**

198 Arp, V. D., McCarty, R. D., & Friend, D. G. (1998). *Thermophysical Properties of Helium-4*

199 *from 0.8 to 1500 K with Pressures to 2000 MPa* (Technical Report No. 1334 (revised)).

200 NIST.

201 Birch, F. (1960). The velocity of compressional waves in rocks to 10 kilobars: 1. *Journal of*

202 *Geophysical Research*, 65(4), 1083–1102. <https://doi.org/10.1029/JZ065i004p01083>

203 Carmichael, R. S. (Ed.). (1989). *Practical handbook of physical properties of rocks and*

204 *minerals*. Boca Raton, Fla: CRC Press.

205 Eberhart-Phillips, D., Han, D.-H., & Zoback, M. D. (1989). Empirical relationships among

206 seismic velocity, effective pressure, porosity, and clay content in sandstone.

207 *GEOPHYSICS*, 54(1), 82–89. <https://doi.org/10.1190/1.1442580>

208 Gassmann, F. (1951). Elastic waves through a packing of spheres. *GEOPHYSICS*, 16(4), 673–

209 685. <https://doi.org/10.1190/1.1437718>

210 Hill, R. (1952). The Elastic Behaviour of a Crystalline Aggregate. *Proceedings of the Physical*
211 *Society. Section A*, 65(5), 349–354. <https://doi.org/10.1088/0370-1298/65/5/307>

212 Hillier, S. (2000). Accurate quantitative analysis of clay and other minerals in sandstones by
213 XRD: comparison of a Rietveld and a reference intensity ratio (RIR) method and the
214 importance of sample preparation. *Clay Minerals*, 35(1), 291–302.
215 <https://doi.org/10.1180/000985500546666>

216 Kerschnitzki, M., Kollmannsberger, P., Burghammer, M., Duda, G. N., Weinkamer, R.,
217 Wagermaier, W., & Fratzl, P. (2013). Architecture of the osteocyte network correlates
218 with bone material quality: OSTEOCYTE NETWORK ARCHITECTURE
219 CORRELATES WITH BONE MATERIAL QUALITY. *Journal of Bone and Mineral*
220 *Research*, 28(8), 1837–1845. <https://doi.org/10.1002/jbmr.1927>

221 Komadel, P., Schmidt, D., Madejová, J., & Čičel, B. (1990). Alteration of smectites by
222 treatments with hydrochloric acid and sodium carbonate solutions. *Applied Clay Science*,
223 5(2), 113–122. [https://doi.org/10.1016/0169-1317\(90\)90017-J](https://doi.org/10.1016/0169-1317(90)90017-J)

224 Lafuente, B., Downs, R. T., Yang, H., & Stone, N. (2015). 1. The power of databases: The
225 RRUFF project. In T. Armbruster & R. M. Danisi (Eds.), *Highlights in Mineralogical*
226 *Crystallography* (pp. 1–30). DE GRUYTER. [https://doi.org/10.1515/9783110417104-](https://doi.org/10.1515/9783110417104-003)
227 003

228 Lee, T. C., Kashyap, R. L., & Chu, C. N. (1994). Building Skeleton Models via 3-D Medial
229 Surface Axis Thinning Algorithms. *CVGIP: Graphical Models and Image Processing*,
230 56(6), 462–478. <https://doi.org/10.1006/cgip.1994.1042>

231 Meredith E. Ostrom (2). (1961). Separation of Clay Minerals from Carbonate Rocks by Using
232 Acid. *SEPM Journal of Sedimentary Research, Vol. 31*.
233 <https://doi.org/10.1306/74D70B1E-2B21-11D7-8648000102C1865D>

234 Moore, D. M., & Reynolds, R. C. (1997). *X-ray diffraction and the identification and analysis of*
235 *clay minerals* (2nd ed). Oxford ; New York: Oxford University Press.

236 Ortiz-Vega, D., Hall, K., Holste, J., Arp, V., Harvey, A., & Lemmon, E. (2020). Helmholtz
237 equation of state for helium. *Journal of Physical and Chemical Reference Data*.

238 Prelicz, R. M. (2005). *Seismic anisotropy in peridotites from the Western Gneiss Region*
239 *(Norway): laboratory measurements at high PT conditions and fabric based model*
240 *predictions* [Application/pdf]. ETH Zurich. <https://doi.org/10.3929/ETHZ-A-005115293>

241 Tsuji, T., & Iturrino, G. J. (2008). Velocity-porosity relationships in oceanic basalt from eastern
242 flank of the Juan de Fuca Ridge: The effect of crack closure on seismic velocity.
243 *Exploration Geophysics, 39*(1), 41–51. <https://doi.org/10.1071/EG08001>

244